nature synthesis

Article

https://doi.org/10.1038/s44160-025-00758-y

Roll-to-roll synthesis of multielement heterostructured catalysts

Received: 24 March 2024

Accepted: 3 February 2025

Published online: 13 March 2025

Check for updates

Wenhui Shi[1,2,7], Hanwen Liu[1,7], Jianwei Zhang[3], Shenyu Shen[4], Yuhan Wang[5], Yaqing Guo[1], Kaihang Yue[2], Zihui Liang[1], Hao Zhang[1], Lei Zhang[1], Fatang Tan[1], Zhiqiang Liang[3], Yingjun Liu[6], Yaqiong Su[4], Dong Su[5], Yunhui Huang[1], Bao Yu Xia[2] ✉ & Yonggang Yao[1] ✉

Heterostructured catalysts are essential for energy conversion and storage. However, scaling up their synthesis while maintaining precise control over diverse components is challenging. Here we introduce the difference in oxidation potential between metals and carbon as a thermodynamic factor for designing multielement heterostructures. A roll-to-roll carbothermal shock technology was developed to achieve one-step synthesis and continuous manufacturing of multielement heterostructured catalysts. A variety of heterostructured catalysts, from single elements to high-entropy alloys, oxides and their combinations, could be synthesized using this method. In addition, kinetic tunability enables precise control over elemental distributions and helps to identify distinct elemental regions to guide the fine-tailoring of heterostructured catalysts. As a proof of concept, we demonstrated rapid screening of PtCo@La–TiO_2 for alkaline hydrogen evolution. Our work proposes an advanced technology for rapid synthesis, screening and continuous production of multielement heterostructured catalysts.

Heterostructured multielement catalysts have been widely used in various industrial processes, exemplified by Fe@K_2O–Al_2O_3 for ammonia synthesis and PtPdRh@La_2O_3–CeO_2–Al_2O_3 for exhaust gas purification[1–6]. Whereas active metals primarily function as catalysts, tuning adsorption and key reaction steps, the oxide support plays a crucial role beyond mere dispersion and stabilization. Through interactions, such as strong metal–support interactions, the oxide acts as a cocatalyst, enhancing both activity and stability[7,8]. However, conventional fabrication methods, such as impregnation, adsorption, precipitation or ion exchange, rely on multistep processes and often lead to poorly defined interfaces between active components[9–13]. Subsequent processing steps including washing, drying and calcination can further compromise active site accessibility and control over metal–support interactions owing to potential metal aggregation and uneven distribution[14–16]. Although progress has been made in developing multielement alloy[17–21] and oxide[22] catalysts, the formation of thermodynamic phases in their heterostructures and the design of specific interfaces remain poorly understood. This knowledge gap restricts the scalability and practical

[1]State Key Laboratory of Materials Processing and Die and Mould Technology, School of Materials Science and Engineering, Huazhong University of Science and Technology, Wuhan, China. [2]Key Laboratory of Material Chemistry for Energy Conversion and Storage (Ministry of Education), Hubei Key Laboratory of Material Chemistry and Service Failure, School of Chemistry and Chemical Engineering, Huazhong University of Science and Technology, Wuhan, China. [3]State Key Laboratory of Bioinspired Interfacial Materials Science, Institute of Functional Nano & Soft Materials (FUNSOM), Soochow University, Suzhou, China. [4]School of Chemistry, Engineering Research Center of Energy Storage Materials and Devices of Ministry of Education, National Innovation Platform (Center) for Industry-Education Integration of Energy Storage Technology, Xi'an Jiaotong University, Xi'an, China. [5]Beijing National Laboratory for Condensed Matter Physics, Institute of Physics, Chinese Academy of Sciences, Beijing, China. [6]MOE Key Laboratory of Macromolecular Synthesis and Functionalization, Department of Polymer Science and Engineering, Zhejiang University, Hangzhou, China. [7]These authors contributed equally: Wenhui Shi, Hanwen Liu. ✉e-mail: byxia@hust.edu.cn; yaoyg@hust.edu.cn

application of many promising catalysts. The increasing complexity of multielement systems and lack of efficient large-scale fabrication methods further exacerbate this limitation.

Here, we establish a thermodynamic descriptor of ΔG_{Temp}^{M-C}, the difference in oxidation potential between metals and carbon, to guide the multielement heterostructure synthesis. We then develop a roll-to-roll carbothermal shock method (CTS, up to ~7 m min^{-1}) for one-step synthesis and continuous manufacturing of multielement heterostructured catalysts. Utilizing the excellent alloying capabilities of high-temperature CTS and guided by ΔG_{Temp}^{M-C}, we synthesized a diverse range of catalysts, including high-entropy alloys, oxides and their heterostructures, where we also demonstrated fine control over element distribution and identified different elemental zones (metal, oxide and tunable) to rationally construct multielement heterostructures. This rapid synthesis approach enables swift screening of heterostructured catalysts. We identified PtCo anchored on the oxyphilic La-doped TiO_2 support (PtCo@La–TiO_2) as an optimized catalyst for alkaline hydrogen evolution reaction (HER). Notably, large-scale electrodes (10 × 100 cm^2) produced continuously showed consistent structure and performances and can be directly assembled into the electrolyser as an integrated cathode, demonstrating the feasibility of scale-up manufacturing. Our work establishes a thermodynamic guideline and advanced technology for the rapid and cross-scale synthesis of multielement heterostructures, offering promising scalability and applicability across various scenarios of clean energy catalysis.

Results and discussion

Roll-to-roll synthesis of heterostructured catalysts

Figure 1a schematically illustrates the rapid and cross-scale manufacturing of multielement heterostructured catalysts via the roll-to-roll CTS method (Supplementary Figs. 1 and 2). Mixed precursors of alloy and oxide compositions are dropped onto a carbon cloth (CC), which was subjected to induced joule heating[17,22–25]. High-temperature CTS enables uniform alloying in metals and oxides, yet an automatic phase separation between metal and oxide occurs, which is guided by the oxidation potential differences between metals and carbon[17]. Benefitting from the in situ and rapid high-temperature process, the multielement heterostructured catalyst was instantaneously formed with intimacy interfaces.

As shown in Fig. 1b, the commercial CC loaded with metal salt precursors was released at a speed of 7 m min^{-1} to pass through the two graphite rollers. A large current was applied to the CC between the two graphite rollers to induce joule heating to increase the temperature for catalyst synthesis. Owing to electrical heating, the temperature can be easily modulated by adjusting the applied current, and the heating duration is affected by the rolling speed and the distance between the two graphite rollers (Fig. 1c and Supplementary Fig. 3). Simultaneously, the self-supported catalyst was collected on the roller after joule heating (Supplementary Movie 1). As shown in Fig. 1d, a relatively large electrode (10 × 100 cm^2) was continuously manufactured within 10 s. Compared with traditional multistep syntheses of heterostructured catalysts (Supplementary Figs. 4 and 5), our method not only enables rapid catalyst preparation in one step (~0.5 s) but can also generally synthesize a series of catalysts ranging from a single element to high-entropy alloy, oxide and their heterostructures (Fig. 1e and Supplementary Table 1), benefitting from the excellent alloying capability of high-temperature CTS and guided by the elemental oxidation potentials, as discussed later.

Multielement heterostructured catalysts can also be synthesized via conventional CTS in a very short shock time (<1 s) owing to the high-temperature enhanced kinetics. However, such transient heating allows CTS to adapt only to very tiny amounts of material (~1 mg or 1 cm^2) in one batch (Supplementary Fig. 6 and Supplementary Table 2). Consequently, despite being time- and energy-efficient, scaling up conventional CTS for mass production is extremely challenging. By contrast, the roll-to-roll CTS enables the continuous and direct preparation of large-scale electrodes with an ultrafast preparation rate (~7 m min^{-1}), where spatial rolling-induced shock achieves an efficient combination between transient synthesis and continuous manufacturing processes, indicating true industry-level scalability. Compared with previously reported single-batch and large-scale preparation methods such as corrosion engineering, anodization and electrocarbiding, our roll-to-roll CTS offers continuous preparation (up to 7 m min^{-1}) and higher productivity (~116.69 cm^2 s^{-1}) (Fig. 1f and Supplementary Table 2).

Rapid screening of heterostructured catalysts

The multielement heterostructured catalysts, endowed with adjustable compositions and intricate interfaces, are especially suitable for multistep catalytic reactions involving diverse reaction intermediates. Here, we choose a simple case for the alkaline HER to demonstrate this concept. In an alkaline proton-deficient environment, proton production by water adsorption and dissociation is a prerequisite step for hydrogen production, which can be facilitated by oxides owing to their excellent oxophilicity[26,27]. In addition, according to Sabatier's principle, an ideal HER catalyst exhibits intermediate hydrogen binding energy, where the adsorption energy of Pt can be optimized by alloying with traditional metals[28,29]. Rapid and general synthesis, as discussed later, enables us to rapidly screen optimal multielement heterostructured catalysts for the alkaline HER in the PtM_3@M_2–M_1O_x space, where (1) M_1O_x acts as a cocatalyst to facilitate water adsorption and dissociation to generate protons (Volmer step); (2) M_2 doped in M_1O_x (M_2–M_1O_x) can modulate the Volmer step; and (3) M_3-doped Pt (PtM_3) can facilitate proton adsorption and hydrogen desorption (Tafel or Heyrovsky step).

Initially, the impact of different oxide supports was systematically studied for the HER where we screened seven heterostructured catalysts (Pt@M_1O_x, M_1 = Cr, Nb, Ta, Ti, Hf, Zr or La). As shown in Fig. 2a, Pt@TiO_2 exhibited the best HER activity and lowest overpotential at a current density of 10 mA cm^{-2} among all the Pt@M_1O_x catalysts, which may be attributed to the optimal oxophilicity and conductivity of the TiO_2 support (Supplementary Fig. 7a)[10,30,31]. To discern the influence of the oxidation potential (oxophilicity) on the HER performance, a correlation between the overpotential and the relative oxidation potential was established, which shows a volcano-type relationship. As shown in Fig. 2b, Pt@Cr_2O_3, Pt@Nb_2O_5 and Pt@TaO_2 have more positive relative oxidation potentials, whereas Pt@HfO_2, Pt@ZrO_2 and Pt@La_2O_3 have more negative relative oxidation potentials. These samples exhibit lower HER activity, which is probably attributed to the *OH adsorption energy being too strong or too weak, limiting the HER process[26,32]. By contrast, Pt@TiO_2, with a moderate relative oxidation potential, exhibited high HER activity, underscoring the critical role of the relative oxidation potential in alkaline HER performance.

Next, we fine-tuned the relative oxidation potential of the oxide support to enhance the alkaline HER performance of Pt@TiO_2. Foreign species such as Cr and Mo with more positive relative oxidation potentials, as well as La with more negative relative oxidation potentials, were introduced to the support material to form Pt@M_2–M_1O_x (Fig. 2a,b and Supplementary Fig. 7b). Specifically, Pt@La–TiO_2 after La doping has enhanced HER activity, which may be attributed to the moderate *OH adsorption energy that promotes the HER process. Finally, conforming to Sabatier's principle[33,34], transition metals (Fe, Co, Ni and Cu) were used to alloy with primary-catalyst Pt metal to form PtM_3@M_2–M_1O_x. The second metal can modify the electronic structure and binding energy of Pt with H* (Fig. 2a,b and Supplementary Fig. 7c), thus contributing to proton adsorption and hydrogen desorption. This resulted in our optimal catalyst PtCo@La–TiO_2 for alkaline HER.

Structure characterization of PtCo@La–TiO_2

The microstructure and morphology of the screened PtCo@La–TiO_2 catalysts were further investigated. First, a large-scale commercial CC

https://doi.org/10.1038/s44160-025-00758-y

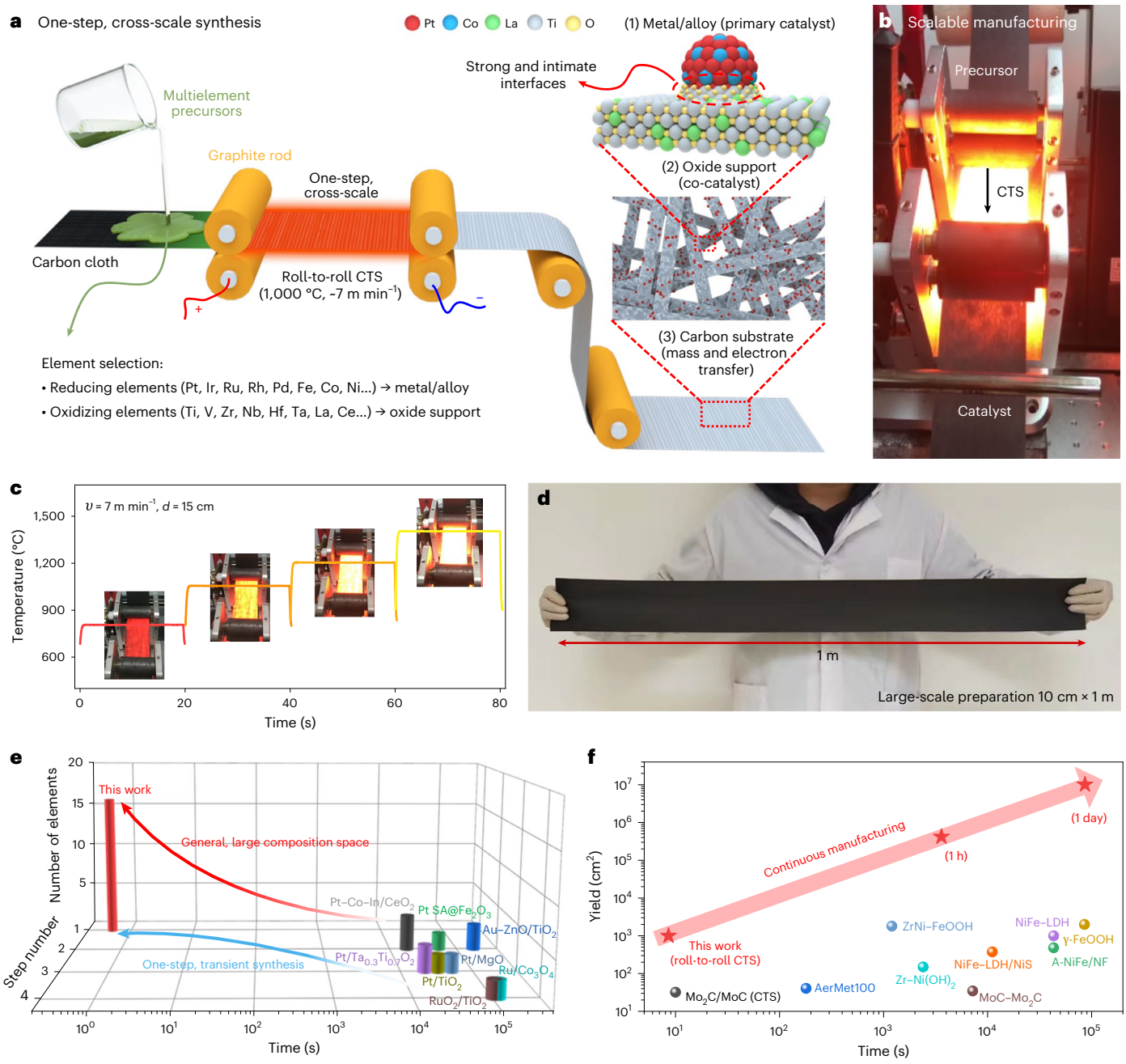

Fig. 1 | Roll-to-roll synthesis of heterostructured catalysts. a, Schematic synthesis of metal@oxide heterostructured catalysts by the roll-to-roll method. **b**, A photograph of the synthesis process. **c**, The corresponding temperature profile at different applied currents of 25 A, 30 A, 35 A and 40 A and a constant speed of 7 m min^{-1} and distance of 15 cm. **d**, A digital photo of a large-scale electrode (10 cm × 100 cm) manufactured via the roll-to-roll synthesis method. **e**, Comparison between traditional synthesis and our one-step synthesis for heterostructured catalysts. **f**, Comparison of efficiency and yield between our roll-to-roll CTS process and the traditional large-scale preparation.

substrate (10 × 100 cm^2) shows an open and porous structure (approximately tens of micrometres) (Fig. 2c,d), enhancing water and electrolyte immersion and facilitating mass and electron transport. To fine-tune the HER performance, we optimized the synthesis temperature (Supplementary Fig. 8) and metal and oxide loading (Supplementary Figs. 9–14), where we found that the optimal temperature (1,000 °C) improved the distribution of La–TiO_2 and that 0.5% PtCo and 7.5% La–TiO_2 are appropriate dosages for superior dispersion and catalytic performance. The actual loading masses are 0.046, 0.0014, 0.36 and 0.12 mg cm^{-2} for Pt, Co, Ti and La, respectively, via inductively coupled plasma mass spectrometer experiments, where the loading amounts of PtCo and La–TiO_2 are 0.474 wt.% and 7.43 wt.% of CC, respectively.

As shown in Fig. 2e, the hierarchically structured PtCo@La–TiO_2 catalysts are attached to the carbon fibre surface, and the PtCo nanoparticles (bright dots) are evenly dispersed on the La-doped TiO_2 island support, which is beneficial for active site exposure. In the transmission electron microscopy (TEM) images (Fig. 2f), the high-density PtCo nanoparticles with a size of ~3.8 nm are uniformly anchored on porous La–TiO_2, directly connected to the carbon substrate and conducive to electron transport, electrolyte immersion and gas release (Supplementary Fig. 15a). These results indicate that the cross-scale PtCo@La–TiO_2 multielement heterostructured catalysts from the nanoscale to the microscale have been successfully prepared. The high-magnification TEM image shows that the particles are trapped in the oxide substrate

https://doi.org/10.1038/s44160-025-00758-y

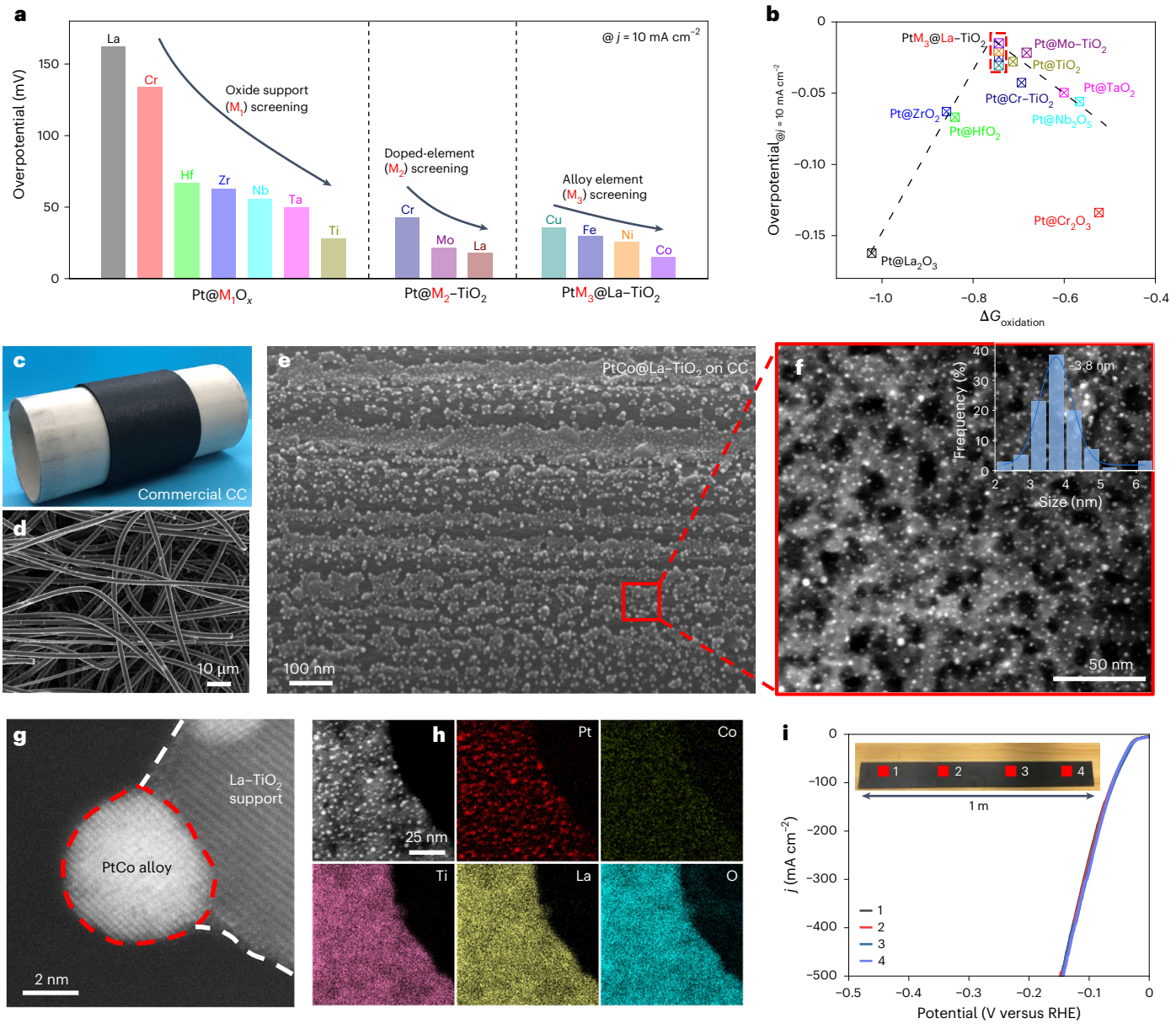

Fig. 2 | Rapid screening and structure characterization of multielement heterostructures. a, Screening and overpotential of $PtM_3@M_2–M_1O_x$ at a current density of 10 mA cm^{-2}. **b**, Volcano plot between the overpotential and the relative oxidation potential of $PtM_3@M_2–M_1O_x$. The black dashed line indicates the 'volcano'-type relationship. The red dashed line includes samples in $PtM_3@La\text{-}TiO_2$, where M_3 = Cu, cyan; Fe, blue; Ni, orange; and Co, lilac. **c**, A photograph of CC. **d**, A scanning electron microscopy (SEM) image of CC. **e**, An SEM image of PtCo@La–TiO_2. **f**, TEM images of PtCo@La–TiO_2. **g**, A high-resolution TEM image of PtCo@La–TiO_2. **h**, High-angle annular dark field scanning TEM (HAADF-STEM) and EDS mapping images of PtCo@La–TiO_2. **i**, LSV curves of PtCo@La–TiO_2 at four different areas.

(Supplementary Fig. 15b), with *d*-spacing of 0.225 nm and 0.354 nm, which are attributed to the Pt (111) and anatase TiO_2 (101) lattice sets[35,36] and are slightly larger than the interplanar spacing of pristine TiO_2, indicating that the lattice defects are caused by the La dopant (Fig. 2g and Supplementary Fig. 15c). According to the energy-dispersive spectroscopy (EDS) maps (Fig. 2h and Supplementary Fig. 16), the Pt and Co elements were confined to the nanoparticle region, whereas the Ti, La and O elements were distributed throughout the entire area, further confirming that the PtCo alloy nanoparticles were distributed on the La–TiO_2 support to form PtCo@La–TiO_2.

The crystal structure, electronic structure and chemical state of the catalysts were further investigated. The anatase TiO_2 was obtained via CTS[37], and La doping induced more oxygen vacancies (O_v) in PtCo@La–TiO_2 (ref. 38) (Supplementary Fig. 18). As shown in Supplementary Fig. 19, the binding energy of Pt 4*f* in PtCo@La–TiO_2 shifts to a lower binding energy compared with PtCo@TiO_2, indicating that La doping promotes electron transfer from La-doped TiO_2 to Pt and verifying the strong interactions between PtCo and the La–TiO_2 support[39]. The heterovalent dopant La^{3+} in TiO_2 can easily form oxygen vacancies (Supplementary Fig. 20a)[40]. For O 1*s* (Supplementary Fig. 20b), the peak located at 531.58 eV is attributed to the oxygen vacancy[41]. For Ti 2*p* (Supplementary Fig. 20c), the Ti^{4+} in PtCo@TiO_2 shifts to lower binding energies compared with PtCo@La–TiO_2, probably owing to the introduction of more oxygen vacancies[42]. Furthermore, according to the electrochemical impedance spectroscopy analysis (Supplementary Fig. 21 and Supplementary Table 3), PtCo@La–TiO_2 exhibited the smallest charge-transfer resistance among all the catalysts. Thus, the introduced oxygen vacancies can tune the electronic structure of

the alloy catalysts, promoting charge transfer and thereby improving electrocatalytic performance.

To optimize large-scale manufacturing, we adjusted the rolling rate to 7 m min^{-1} and determined that 1,000 °C and a 5 cm distance yielded the optimal electrode via roll-to-roll CTS (Supplementary Figs. 22–25). To achieve reproducibility and uniformity, we analysed four different areas from the central portions of the large electrode. These areas showed a homogeneous distribution of PtCo nanoparticles on La–TiO_2 island supports with consistent particle sizes and distributions (Supplementary Figs 26–28). X-ray diffraction patterns confirmed the presence of anatase TiO_2 without the characteristic Pt signals (Supplementary Fig. 29), and no Cl signals were observed in the large-scale PtCo@La–TiO_2 (Supplementary Fig. 30), indicating complete precursor decomposition. Importantly, all four areas exhibited consistent electrochemical HER performance (Fig. 2i), emphasizing the robust reproducibility of the roll-to-roll synthesis method. We further investigated the uniformity of the edge portion for the large electrode. Supplementary Figs. 31 and 32 show the uniform dispersion of hierarchically structured PtCo@La–TiO_2 catalysts across the upper and lower edge portions, consistent with the central part. This large-area uniformity is primarily attributed to the uniform roll-to-roll heating process in our approach.

Catalytic evaluation of heterostructured PtCo@La–TiO_2

The electrocatalytic HER performance of the as-prepared samples was thoroughly assessed through a three-electrode configuration in a 1.0 M KOH electrolyte. The incorporation of La enhanced the HER activity of PtCo@La–TiO_2, as indicated by the linear scanning voltammograms (LSVs) in Fig. 3a. PtCo@La–TiO_2 exhibited commercial Pt/C-like activity with an overpotential of 15 mV at a current density of 10 mA cm^{-2}, which is lower than that of Pt/C (24 mV), Pt (62 mV) and PtCo@TiO_2 (27 mV) (Fig. 3b). Moreover, the current density of PtCo@La–TiO_2 at a potential of −0.1 V reached 189 mA cm^{-2}, surpassing that of commercial Pt/C (80 mA cm^{-2}), Pt (22 mA cm^{-2}) and PtCo@TiO_2 (122 mA cm^{-2}). Notably, PtCo@La–TiO_2 exhibited a smaller Tafel slope (19.8 mV dec^{-1}) compared with that of commercial Pt/C (64.4 mV dec^{-1}), Pt (117.4 mV dec^{-1}) and PtCo@TiO_2 (43.8 mV dec^{-1}) (Fig. 3c), indicating a much faster HER kinetics process that follows an efficient Volmer–Tafel mechanism[43]. Besides, the alkaline HER activity of PtCo@La–TiO_2 exceeds that of most other recently reported Pt-based catalysts (Supplementary Table 4).

Although the surface area of PtCo@La–TiO_2 increased by 1.3 times compared with that of PtCo@TiO_2 (Supplementary Figs. 33 and 34), the specific activity of PtCo@La–TiO_2 was still greater than that of PtCo@TiO_2 (Supplementary Fig. 35), suggesting that the superior HER performance of PtCo@La–TiO_2 comes from not only an increased surface area but also an increase in intrinsic activity. Moreover, the TOF value of the PtCo@La–TiO_2 electrode (2.39 s^{-1} at an overpotential of 70 mV) is higher than that of PtCo@TiO_2 (1.34 s^{-1}), Pt/C (0.95 s^{-1}) and Pt (0.26 s^{-1}) (Supplementary Fig. 36), indicating the high intrinsic HER activity of PtCo@La–TiO_2. Compared with commercial Pt/C with a large voltage drop (212 mV), PtCo@La–TiO_2 demonstrated a negligible voltage drop (38 mV) after 100 h (Supplementary Fig. 37), indicating excellent electrochemical stability, which is also comparable to that of state-of-the-art Pt-based catalysts (Supplementary Fig. 38). Microstructure examination of the post-stability test (Supplementary Fig. 39) revealed that, unlike the notable particle aggregation in commercial Pt/C, the morphology of PtCo@La–TiO_2 remained unaltered, indicating that the La–TiO_2 support enhances the stability of the PtCo nanoparticles through the strong metal–support interaction.

To elucidate the role of heterostructured PtCo@La–TiO_2 in the alkaline HER, we systematically investigated the catalytic processes of water adsorption, dissociation, proton adsorption and hydrogen desorption via both experimental and theoretical methods. The PtCo@La–TiO_2 electrode exhibits more aerophobic and superhydrophilic characteristics (Supplementary Fig. 40 and Supplementary Movies 2–5), attributed to the hierarchical structure surface and oxyphilic La doping[44,45]. Moreover, spin-polarized density functional theory calculations were used to reveal the influence of La doping and oxygen vacancies on the enhanced alkaline HER of PtCo@La–TiO_2 (Supplementary Figs. 41 and 42). The electron transfers from La–TiO_2 to the PtCo cluster (Supplementary Fig. 43), demonstrating the formation of the electron-rich PtCo cluster in PtCo@La–TiO_2. Furthermore, compared with that of PtCo@TiO_2, the *d*-band centre for Pt in PtCo@La–TiO_2 shifts farther to the Fermi energy level by 0.12 eV (Supplementary Fig. 44). According to the *d*-band centre theory, a downshift of the *d*-band centre usually leads to weakened H* adsorption, thus promoting hydrogen spillover and eventually H_2 production[46,47]. In alkaline electrolytes, favourable water adsorption and dissociation kinetics are prerequisites for the HER and directly determine the HER activity[48–51]. The introduction of the oxide support and La doping strengthened the binding of water molecules to PtCo@La–TiO_2 (Supplementary Fig. 45). We further calculated the kinetic-energy barrier of water dissociation for PtCo@TiO_2 and PtCo@La–TiO_2 (Fig. 3d). Notably, the energy barrier of water dissociation in PtCo@La–TiO_2 (0.1 eV) is much lower than that in PtCo@TiO_2 (0.79 eV), indicating that doping the La atoms into TiO_2 can promote the cleavage of the HO–H bond to form *H intermediates. PtCo@TiO_2 demonstrated a weaker adsorption free energy (−0.78 eV) due to the electron transfer from the TiO_2 support to the PtCo cluster (Supplementary Fig. 46).

Figure 3e shows the free energy values of HER on the Pt site (cyan line) and O_v site through the hydrogen spillover pathway (red line) for PtCo@La–TiO_2. The ΔG_{H^*} value on the hollow sites of the PtCo cluster is −0.31 eV, which subsequently diffuses to the interface site between the Pt atom and O_v, providing a ΔG_{H^*} value of 0.04 eV, accounting for the facile hydrogen evolution. In essence, the alkaline HER on the PtCo@La–TiO_2 surface involves the dissociation of H_2O at the Pt site, hydrogen spillover from the Pt site to the O_v site and efficient hydrogen desorption on the O_v site. Therefore, as schematically illustrated in Supplementary Fig. 47, La doping into the TiO_2 support enhances the water adsorption capability, lowers the energy barrier of water dissociation and promotes hydrogen spillover from the PtCo alloy to the O_v site of the La–TiO_2 support, synergistically enhancing the electrocatalytic hydrogen-evolution activity.

Furthermore, to assess the application potential of the PtCo@La–TiO_2 catalyst, an anion-exchange-membrane (AEM) water electrolyser was assembled, using the large-scale PtCo@La–TiO_2 (Pt mass loading ~0.05 mg cm^{-2}) and NiFe@NF as the cathode and anode electrodes (Fig. 3f), respectively. PtCo@La–TiO_2 and commercial Pt/C powder catalysts were sprayed on the carbon paper, forming S–PtCo@La–TiO_2 and S–Pt/C (Pt mass loading ~0.3 mg cm^{-2}) electrodes. As shown in Fig. 3g, the PtCo@La–TiO_2||NiFe@NF electrolyser exhibited improved catalytic activity, and required a cell voltage of 1.85 V to reach a current density of 1,000 mA cm^{-2}, which is comparable to those of advanced AEM electrolysers (Supplementary Table 5) and lower than those of the S–PtCo@La–TiO_2||NiFe@NF (1.94 V@1,000 mA cm^{-2}), yet the S–Pt/C||NiFe@NF electrolyser required a higher cell voltage (2.2 V) to reach a low current density (500 mA cm^{-2}). We also assembled AEM electrolysers with different electrode sizes of 1 × 1, 2 × 2 and 5 × 5 cm^2 (Supplementary Fig. 48), where they all exhibited similar HER performance, indicating that the performance of our roll-to-roll prepared electrodes is consistent in electrolysers.

Moreover, the long-term stability of the PtCo@La–TiO_2||NiFe@NF electrolyser was tested at a current density of 1,000 mA cm^{-2} (Fig. 3h), which maintained a nearly constant cell voltage during long-term operation for 100 h without obvious degradation. However, the cell voltages of the S–PtCo@La–TiO_2||NiFe@NF and S–Pt/C||NiFe@NF electrolysers increased after 50 h at 1,000 mA cm^{-2} and after 30 h at 400 mA cm^{-2}, respectively, further verifying the advantages of the PtCo@La–TiO_2 electrode. In addition, a water-drainage method was used to collect the volume of H_2 produced by the PtCo@La–TiO_2 catalyst. As shown in Supplementary Fig. 49, the Faradaic efficiency was estimated to be

https://doi.org/10.1038/s44160-025-00758-y

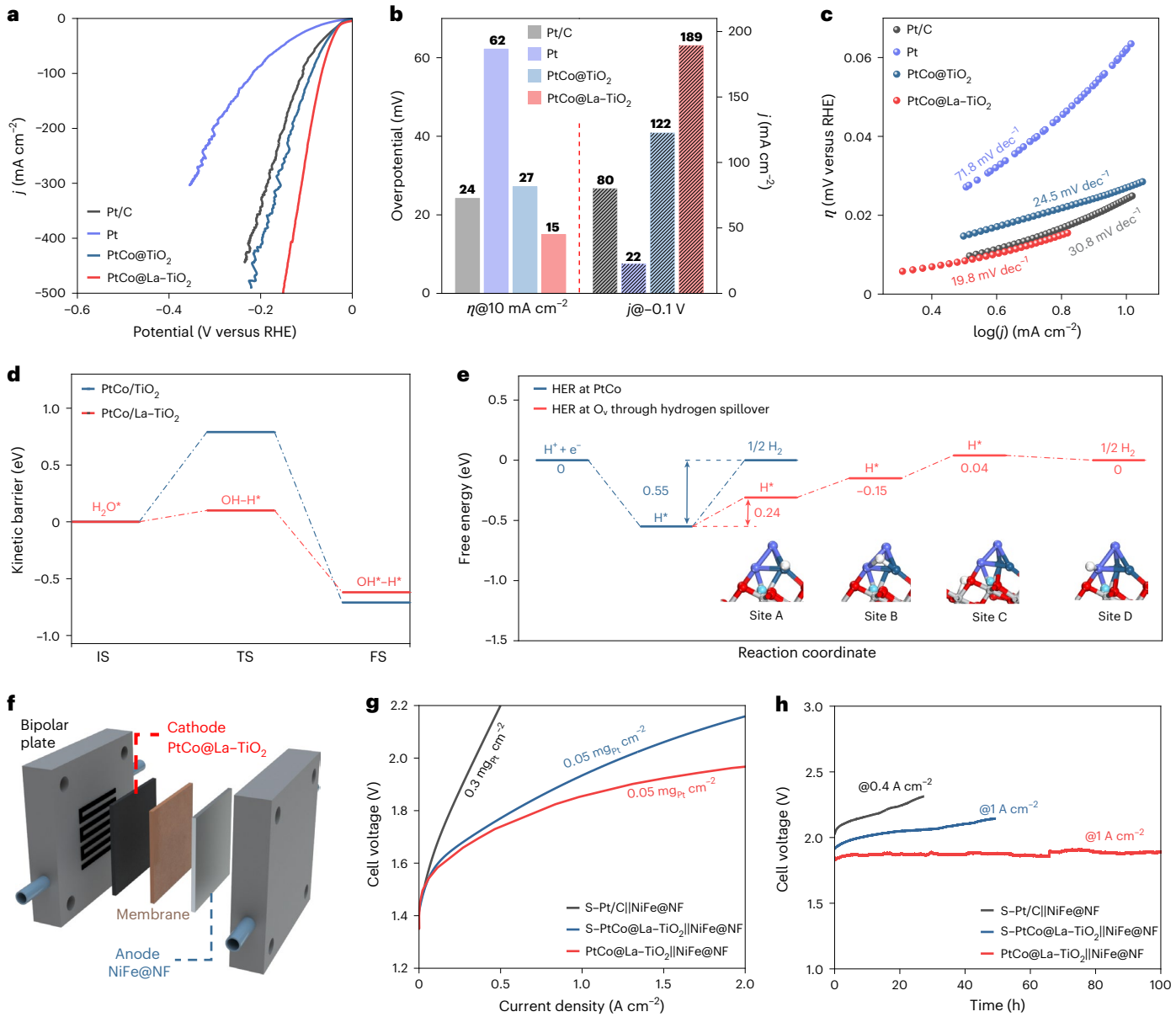

Fig. 3 | HER performance of PtCo@La–TiO_2 catalyst. a, LSV curves of Pt/C, Pt, PtCo@TiO_2 and PtCo@La–TiO_2. **b**, Overpotential at 10 mA cm^{-2} and current density at −0.1 V versus RHE for Pt/C, Pt, PtCo@TiO_2 and PtCo@La–TiO_2. **c**, The corresponding Tafel slopes. **d**, The kinetic barrier of water dissociation of different catalysts. IS, initial state; TS, transition state; FS, final state. **e**, Gibbs free energy diagram for the HER at the Pt atom and O_v through the hydrogen spillover pathway for PtCo@La–TiO_2. **f**, Schematic of an AEM water electrolyser. **g**,**h**, Polarization curves (**g**) and chronopotentiometry tests (**h**) of the AEM water electrolyser using PtCo@La–TiO_2 or Pt/C as the cathodic catalysts and NiFe@NF as the anodic catalyst in a 1.0 M KOH solution.

close to 90% by comparing the measured and calculated volumes of hydrogen generation. The above scenario also enables us to rapidly optimize the catalysts for harsh alkaline oxygen evolution reaction (OER) via a multielement heterostructured design (Supplementary Fig. 50) where FeCoNiCrMn@HfMoWZrCeO_x exhibited the lowest overpotential of 265 mV at 100 mA cm^{-2} and long-term stability (~250 h without obvious degradation), indicating the importance of a multielement heterostructured design for improving the catalytic performance even in the harsh alkaline OER.

Thermodynamic guidance and general synthesis

To elucidate the formation mechanism of multielement heterostructured catalysts, we analysed the Ellingham diagram[52,53] (Supplementary Fig. 51). Sign differences in the oxidation potentials of elements facilitate phase separation between metals (primary catalysts) and oxide supports (dispersion, stabilization and cocatalysts) during the CTS process. We extracted the oxidation potential values of each metal element (M, ΔG^{M}_{Temp}) and carbon (C, ΔG^{C}_{Temp}) at a specific temperature (Temp) from the Ellingham diagram. Then, we calculated the oxidation potential differences between the metal element and carbon ($\Delta G^{M-C}_{Temp} = \Delta G^{M}_{Temp} - \Delta G^{C}_{Temp}$). We identified the ΔG^{M-C}_{Temp} as a thermodynamic descriptor to guide the synthesis of heterostructured catalysts. For example, as shown in Fig. 4a and Supplementary Table 6, we compared the ΔG^{M-C}_{Temp} of each element with the carbon oxidation potential at 1,000 °C, where a positive $\Delta G^{M-C}_{1,000}$ (marked in red) means easy reduction and alloying by CTS, and conversely, a more negative $\Delta G^{M-C}_{1,000}$ (marked in blue) means easy oxidation to form oxide supports. In a multielement system, sign differences in ΔG^{M-C}_{Temp} induce natural phase separation between metal and oxide support, enabling the one-step in situ synthesis of multielement heterostructures.

https://doi.org/10.1038/s44160-025-00758-y

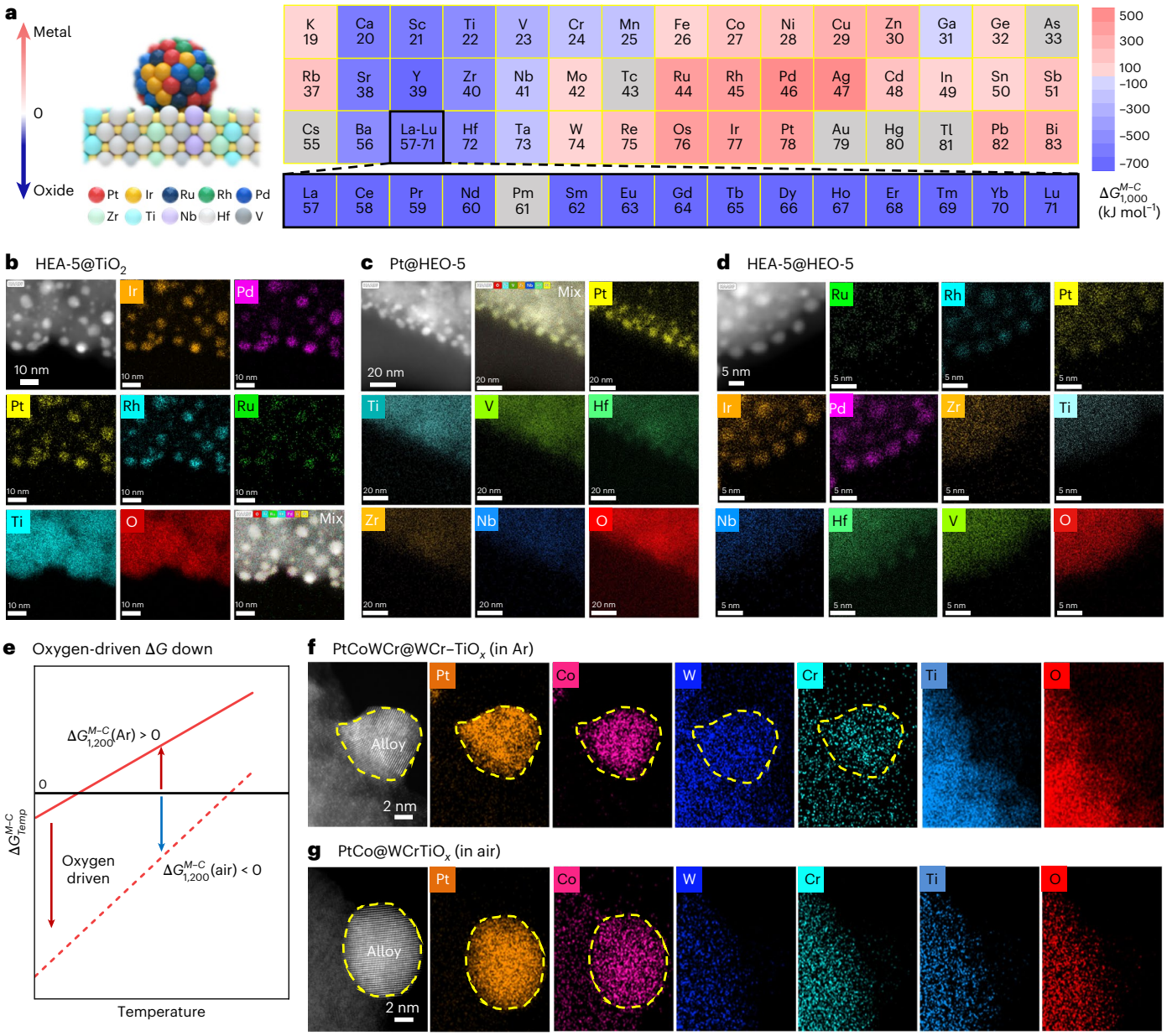

Fig. 4 | Thermodynamic guideline and general synthesis of multielement heterostructures. a, Thermodynamic descriptor of ΔG^{M-C}_{Temp} in the periodic table at 1,000 °C. Data source: ref. 54. **b**–**d**, The HAADF-STEM and EDS mapping images of HEA-5@TiO_2 (**b**), Pt@HEO-5 (**c**) and HEA-5@HEO-5 (**d**). **e**, Variation of the calculated ΔG^{M-C}_{Temp} in Ar and air. **f**,**g**, The HAADF-STEM and EDS mapping images of PtCoWCr@WCr−TiO_x (**f**, in Ar) and PtCo@WCrTiO_x (**g**, in air).

As a result, a series of multielement alloy/oxide catalysts (such as Pt@HEO-5, HEA-5@TiO_2 and HEA-5@HEO-5) are generally synthesized in a single step, where the in-situ-formed heterostructures exhibit strong and intimate interfaces compared with the metal-on-support structures often reported in the literature. Benefitting from the high-temperature CTS process, the multielement heterostructured catalyst was instantaneously formed with metal–support interfaces. For example, (1) for multielement alloy@oxide heterostructure, as shown in Fig. 4b and Supplementary Fig. 52, the Pt, Ir, Ru, Rh and Pd signals were confined within the particle area, whereas the Ti and O signals were distributed throughout the particle area, indicating that the PtIrRuRhPd multielement high-entropy alloy nanoparticles (HEAs) were loaded on the TiO_2 support and formed HEA-5@TiO_2; (2) for metal@multielement oxide heterostructure, Fig. 4c and Supplementary Fig. 53 reveal that the Zr, Ti, Nb, Hf, V and O signals are distributed across the entire region, with Pt signals located in the particle areas, indicating that the Pt particles anchored on the ZrTiNbHfVO_x multielement high-entropy oxide support (HEO) and formed Pt@HEO-5; (3) for multielement alloy@multielement oxide heterostructure, as shown in Fig. 4d and Supplementary Fig. 54, the EDS mapping images demonstrate that the PtIrRuRhPd nanoparticles were distributed on the ZrTiNbHfVO_x support and formed HEA-5@HEO-5, indicating the general synthesis of various heterostructured catalysts with widely tunable compositions and metal–support interface.

We also observed that increasing oxygen partial pressure decreases the oxidation potential (Fig. 4e and Supplementary Fig. 55). This can cause the oxidation potential difference of certain elements to shift from positive to negative at higher oxygen bias, inducing a transition from a reducing state to an oxidizing state. To verify this effect, we synthesized PtCoWCrTi catalysts under different atmospheres. Under the Ar atmosphere (Fig. 4f), Pt and Co formed metal particles, while Ti and O formed oxide supports. Notably, W and Cr were present in both metallic

https://doi.org/10.1038/s44160-025-00758-y

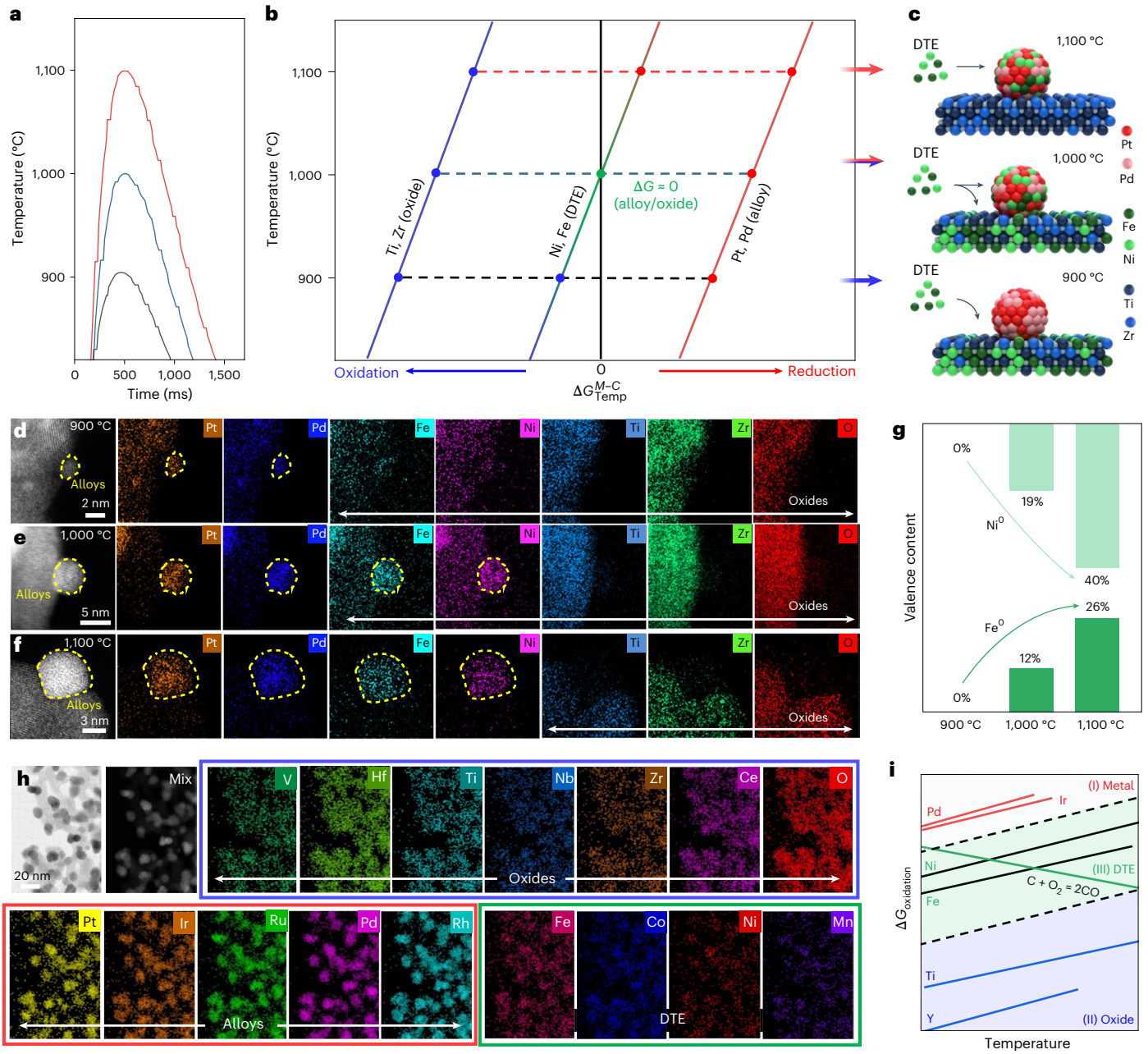

Fig. 5 | Dynamic tunability and element guideline map of multielement heterostructures. a, The kinetically tunable temperature of the CTS process (red, ~1,100 °C; navy blue, ~1,000 °C; black, ~900 °C). **b**, The temperature dependence of $\Delta G^{M-C}_{oxidation}$. **c**, Schematic diagram of element dynamic regulation. **d**–**f**, HAADF-STEM and **d** EDS mapping of PtPd@FeNiTiZrO$_x$ (**d**), PtPdNiFe@FeNi–TiZrO$_x$ (**e**) and PtPdNiFe@TiZrO$_x$ (**f**). **g**, The valence content of Ni^0 and Fe^0 at different temperatures (900, 1,000 and 1,100 °C). **h**, HAADF-STEM and EDS mapping images of HEA-9@HEO-10. **i**, Element guideline map of multielement heterostructured catalyst: (1) metal/alloy area, (2) oxide area and (3) DTE area.

and oxide phases, resulting in PtCoWCr anchored on WCr-doped TiO$_x$ in the PtCoWCr@WCr–TiO$_x$ structure. By contrast, under air atmosphere (Fig. 4g), Pt and Co formed metal particles, while W, Cr, Ti and O formed oxide supports due to the complete oxidation of W and Cr, leading to the PtCo@WCrTiO$_x$ structure with PtCo anchored on WCrTiO$_x$ support. These findings demonstrate the large influence of oxygen partial pressure on the formation of multielement heterostructure and its tunability of elemental distribution between metal and oxide phases.

Dynamic tunability and element guideline map

Although the interface interaction and reconstruction between metal and oxide support has been extensively studied[4–6], the regulation of element distribution within heterostructured catalysts, especially in multielement systems, remains relatively unexplored. Here, we revealed the temperature sensitivity of ΔG^{M-C}_{Temp}, which provides a robust basis for finely controlling the element distribution in the multielement heterostructures through kinetic manipulation. We discovered that the metal/oxide behaviours can be greatly influenced by the CTS temperature, especially for elements with ΔG^{M-C}_{Temp} values near zero, allowing them to undergo either reduced or oxidized states with dynamic tunability. The element distributions can be kinetically tuned via the precise CTS process to enable dynamic tunable elements (DTE), where these elements can migrate from the oxide to alloy regions with increasing CTS temperatures (Fig. 5a–c).

As shown in Fig. 5d–f and Supplementary Fig. 56, the Pt and Pd were confined to specific areas in the metallic particle areas at different temperatures, whereas the Ti and Zr signals were distributed throughout the oxide supports. Interestingly, the Fe and Ni signals are temperature dependent: (1) during high-temperature CTS (1,100 °C), they were primarily located in the particle areas; (2) during low-temperature CTS (900 °C), they were distributed throughout the oxide support; and (3) during moderate-temperature CTS (1,000 °C), they were not only dispersed in the particle areas but also located in the oxide support, indicating their dynamic tunability between the metal nanoparticles and the oxide support, resulting in the synthesis of PtPd@FeNiTiZrO$_x$, PtPdFeNi@TiZrO$_x$ and PtPdFeNi@FeNi–TiZrO$_x$. Furthermore, X-ray photoelectron spectroscopy was used to investigate the content of Ni and Fe in both metallic and oxide states. As shown in Fig. 5g, the metallic Ni and Fe content increases with increasing temperature, consistent with the EDS mapping results (Supplementary Fig. 57).

Furthermore, Fe, Co, Ni, Mo, W and Sn are positioned in proximity to the carbon oxidation curves (Supplementary Fig. 51), signifying that their metal/oxide behaviours can be influenced by the CTS temperature, allowing them to undergo either reduction or oxidation with dynamic tunability. For example, a more flexible and adjustable multielement alloy@oxide heterostructured catalyst was designed. As shown in Fig. 5h, the Pt, Ir, Ru, Rh and Pd elements were confined to specific areas in the metallic particle areas, while the Zr, Ti, Nb, Hf, V, Ce and O signals were distributed throughout the oxide supports. Interestingly, the Fe, Co, Ni and Mn signals are primarily located in the particle areas, with some remaining signals distributed across the entire area, indicating their dynamic tunability in both the metal nanoparticles and the oxide support, resulting in PtIrRuRhPdFeCoNiMn anchored on FeCoNiMn-doped ZrTiNbHfVCeO$_x$ (HEA-9@HEO-10; Supplementary Figs. 58 and 59). These heterostructured materials, with a vast range of components and multiple active sites, are well suited for various multistep catalytic reactions. Based on the above results, we divided elements into three categories: (1) metal/alloy area ($\Delta G^{M-C}_{\mathrm{Temp}} > 0$ at any temperature), (2) oxide area ($\Delta G^{M-C}_{\mathrm{Temp}} < 0$ at any temperature) and (3) DTE area ($\Delta G^{M-C}_{\mathrm{Temp}}$ changes from positive to negative with increasing temperature) (Fig. 5i), where an elemental guiding map was developed for fine-tailoring multielement metal-oxide heterostructured catalysts.

Conclusion

In summary, we revealed the formation mechanism of multielement heterostructures and proposed $\Delta G^{M-C}_{\mathrm{Temp}}$, the difference in oxidation potential between metals and carbon, as a thermodynamic descriptor to guide the design and synthesis of the multielement heterostructure. A roll-to-roll CTS technology was developed to realize the rapid and large-scale preparation of multielement heterostructured catalyst at ~7 m min^{-1} continuously. Guided by the $\Delta G^{M-C}_{\mathrm{Temp}}$, a series of multielement heterostructured catalysts, including HEA-5@TiO$_2$, Pt@HEO-5, HEA-5@HEO-5 and HEA-9@HEO-10, were generally synthesized. In addition, the element distribution was kinetically manipulated, and different elemental zones (metal, oxide or tunable) were further identified to rationally construct multielement heterostructures. This work examines a thermodynamic guideline and advanced manufacturing approach to the rapid synthesis and cross-scale manufacturing of multielement heterostructured catalysts, presenting promising scalability and applicability across various multistep catalytic processes.

Methods

Chemical and materials

The CC (SCF210) and carbon paper (TGP-H-060) used in the electrocatalysis tests were purchased from Suzhou Shengernuo. All the chemicals were purchased from Shanghai Aladdin Biochemical Technology. Salts, including $TiCl_4$ (99.0%), VCl_3 (96.0%), $NbCl_5$ (99.0%), $MoCl_5$ (99.0%), WCl_5 (99.0%), $TaCl_5$ (99.0%), $ZrCl_4$ (98.0%), $HfCl_4$ (99.5%), $Ce(NO_3)_3{\cdot}6H_2O$ (99.0%), $La(NO_3)_3{\cdot}6H_2O$ (99.0%), $Mn(NO_3)_2{\cdot}4H_2O$ (98.0%), $Cr(NO_3)_3{\cdot}9H_2O$ (99.0%), $Fe(NO_3)_3{\cdot}9H_2O$ (98.0%), $Co(NO_3)_2{\cdot}6H_2O$ (98.0%), $Ni(NO_3)_2{\cdot}6H_2O$ (98.0%), $H_2PtCl_6{\cdot}xH_2O$ (99.95%), $RuCl_3{\cdot}xH_2O$ (99.9%), $RhCl_3$ (98.0%), $PdCl_2$ (99.9%) and $IrCl_3$ (99.8%), were dissolved in ethanol solution to prepare the different salt solutions (0.05 mol l^{-1}).

Material preparation

For the preparation of a PtCo@La–TiO$_2$ electrode, commercial CC (0.5 × 3 cm^2, 15 mg) was cleaned in ethanol, diluted with HCl and ultrapure water, and then dried at room temperature. The estimated loading masses for PtCo and La–TiO$_2$ are 0.5 wt.% and 7.5 wt.%, respectively, of CC. The precursors containing 0.5 wt.% Pt:Co = 9:1 (7.2 µl 0.05 mol l^{-1} H_2PtCl_6 and 4 µl 0.01 mol l^{-1} $CoCl_2$) and 7.5 wt.% Ti:La = 9:1 (270 µl 0.05 mol l^{-1} $TiCl_4$ and 30 µl 0.05 mol l^{-1} $La(NO_3)_3$) were dropped onto the CC and then dried at room temperature. A pulse current was applied to the CC, followed by joule heating (1,000 °C, 500 ms), and the catalyst was synthesized in an argon-filled glove box. For comparison, the PtCo@TiO$_2$ without La was synthesized by using only Pt, Co and Ti. In addition, the Pt electrode was prepared via a similar method, using only Pt. Other multielement heterostructured catalysts, such as Pt@HEO-5, HEA-5@TiO$_2$, HEA-5@HEO-5 and HEA-9@HEO-10, were synthesized via the same method using the corresponding salt precursor solutions in specific proportions (Supplementary Table 7).

Roll-to-roll manufacturing

The homemade roll-to-roll CTS equipment was constructed by combining CTS technology with a roll-to-roll device, which was driven by an alternating current dynamo. Two graphite rollers (length 12 cm, diameter 4 cm) were used as positive and negative electrodes, and electrical pulses were applied to the CC via the graphite rollers, and the distance between them can be adjusted from 5 to 15 cm. The temperature can be directly detected by an infrared thermometer (SA-D30180A, 300–1,800 °C). The roll-to-roll CTS process was conducted in an argon-filled glovebox. The large-scale CC (10 × 100 cm^2) loaded with the salt precursor (4.8 ml 0.05 mol l^{-1} H_2PtCl_6, 0.53 ml 0.05 mol l^{-1} $CoCl_2$, 9 ml 1 mol l^{-1} $TiCl_4$ and 5 ml 0.2 mol l^{-1} $La(NO_3)_3$.) continuously passed through the two graphite rollers at a distance of 5 cm, driven by an alternating current dynamo at a speed of 7 m min^{-1}. An adjustable d.c. power source (A-BF, SS-6060P) was used to supply a constant current (30 A) across the graphite rollers, achieving a continuous CTS process (1,000 °C) and scalable manufacturing of the catalyst.

Characterizations

SEM was performed at 10 kV on a TESCAN MIRA4 with EDS analysis at 15 kV. X-ray photoelectron spectroscopy was carried out on a Thermo Scientific K-Alpha. EPR spectra were recorded at room temperature using a Bruker EMX spectrometer. X-ray diffraction was performed on a Bruker C2 Discover X-ray powder diffractometer. The temperature of the CC with the salt precursor during the high-temperature shock process was recorded on a Fluke Process Instrument E1RH-R59-V-0-0. TEM images were obtained via an aberration-corrected FEI Titan Themis G2 300 microscope.

Electrochemical measurements

The electrochemical performance was tested in a three-electrode setup with an electrochemical workstation (CS3104, Wuhan Kostec Instrument). A graphite rod, an Ag/AgCl electrode with a saturated potassium chloride solution (Wuhan Gaoshi Rui Lian Technology), and the as-prepared catalysts (0.5 wt.% PtCo and 7.5 wt.% La–TiO$_2$ on carbon) were used as the counter, reference and working electrodes, respectively. The electrolyte used for the HER and OER tests was a 1 M KOH solution.

For the HER test, the catalyst was first activated via the CV method from −1.3 to 1.1 V at scan rates of 50 mV s^{-1} for 100 cycles. The LSV curves

were investigated from −1.5 V to 1.1 V at scan rates of 5 mV s^{-1}. Chronoamperometry was used to test the stability of the catalyst. The stability was measured at a current density of 10 mA cm^{-2} for 100 h. All potentials were compensated by 90% iR (where iR is Ohmic drop) to correct the solution's ohmic resistance. The tested potentials versus the Ag/AgCl reference electrode were converted to a reversible hydrogen electrode (RHE) on the basis of the following equation: $E_{RHE} = E_{Ag/AgCl} + 0.059 \times pH + 0.197$ V.

For overall water splitting, the electrochemical performance was evaluated via the Neware battery test system. The AEM electrolyser was purchased from Wuhan Zhisheng New Energy. The FAA-3-PK-130 anionic membrane was purchased from Suzhou Shengernuo. The membrane was activated by soaking it for 24 h in a 1.0 M KOH solution before use. The membrane was sandwiched between the large-scale PtCo@La–TiO_2 or Pt/C cathode (2 × 2 cm^2) and NiFe-LDH@Ni foam (NiFe@NF) anode (2 × 2 cm^2). For the Pt/C electrode, the catalyst ink was prepared by homogeneously dispensing 10 mg of Pt/C catalyst into ethanol and FAA-PK-130 mixture under sonication at 0 °C for approximately 1 h. Afterwards, 1.2 ml of catalyst ink was sprayed on the carbon paper with an exposed surface area of 4 cm^2. The mass loading was approximately 0.3 mg of Pt per square centimetre. A 1.0 M KOH electrolyte was fed into the AEM electrolyser through a small water pump at a flow rate of 40 ml min^{-1}. The polarization curves were measured at 25 °C under ambient pressure from 1.2 V to 2.2 V. A stability test was performed via galvanostatic electrolysis at 4.0 A constant current at room temperature.

Computational methods

The density functional theory calculations were performed via the Vienna ab initio simulation package (VASP). The exchange–correlation interactions are treated by the Perdew–Burke–Ernzerhof functional. The plane-wave basis set with a kinetic energy cut-off of 400 eV, the energy convergence criterion of 10^{-5} eV, the force convergence criterion of 0.02 eV $Å^{-1}$ and a (2 × 2 × 1) Monkhorst–Pack *k*-point sampling is used for structure relaxation. For different surface models, the bottom layer is fixed. A sufficiently large vacuum gap (>10 Å) is used to prevent the interaction between neighbouring periodic structures along the *c* axis. H_2 and H_2O were calculated in boxes of 20 Å × 20 Å × 20 Å with the gamma point only. The Climbing Image Nudged Elastic Band (CI-NEB) method was adopted to search for the minimum energy paths of the H_2O dissociation reaction. Six images were used for the CI-NEB calculations. The free energy diagrams for the HER were calculated concerning the computational hydrogen electrode. The free energy of the gas phase and adsorbed species can be obtained from

$$\Delta G = \Delta E_{elec} + \Delta ZPE - T\Delta S,$$

where ΔE_{elec} is the electronic energy difference; ΔZPE and Δ*S* are the difference of zero-point energies and the change of entropy, respectively; and *T* is 298.15 K.

Data availability

All the data supporting the conclusions of this study are available within the Article and its Supplementary Information. Source data are provided with this paper.

References

1. Yuan, W. et al. In situ manipulation of the active Au–TiO_2 interface with atomic precision during CO oxidation. *Science* **371**, 517–521 (2021).
2. Cargnello, M. et al. Exceptional activity for methane combustion over modular Pd@CeO_2 subunits on functionalized Al_2O_3. *Science* **337**, 713–717 (2012).
3. Erisman, J. W. et al. How a century of ammonia synthesis changed the world. *Nat. Geosci.* **1**, 636–639 (2008).
4. Beck, A. et al. The dynamics of overlayer formation on catalyst nanoparticles and strong metal–support interaction. *Nat. Commun.* **11**, 3220 (2020).
5. Frey, H. et al. Dynamic interplay between metal nanoparticles and oxide support under redox conditions. *Science* **376**, 982–987 (2022).
6. Monai, M. et al. Restructuring of titanium oxide overlayers over nickel nanoparticles during catalysis. *Science* **380**, 644–651 (2023).
7. Deng, D. et al. Catalysis with two-dimensional materials and their heterostructures. *Nat. Nanotechnol.* **11**, 218–230 (2016).
8. Zhao, G. et al. Heterostructures for electrochemical hydrogen evolution reaction: a review. *Adv. Funct. Mater.* **28**, 1803291 (2018).
9. Kumar, A. et al. Strong metal–support interactions enhance the activity and durability of platinum supported on tantalum-modified titanium dioxide electrocatalysts. *ACS Catal.* **4**, 1516–1525 (2014).
10. Nong, S. et al. Well-dispersed ruthenium in mesoporous crystal TiO_2 as an advanced electrocatalyst for hydrogen evolution reaction. *J. Am. Chem. Soc.* **140**, 5719–5727 (2018).
11. Song, S. et al. A selective Au–ZnO/TiO_2 hybrid photocatalyst for oxidative coupling of methane to ethane with dioxygen. *Nat. Catal.* **4**, 1032–1042 (2021).
12. Vincent, J. L. et al. Atomic level fluxional behavior and activity of CeO_2-supported Pt catalysts for CO oxidation. *Nat. Commun.* **12**, 5789 (2021).
13. Xing, F. et al. Ternary platinum–cobalt–indium nanoalloy on ceria as a highly efficient catalyst for the oxidative dehydrogenation of propane using CO_2. *Nat.Catal.* **5**, 55–65 (2022).
14. Yang, X. et al. Constructing oxygen vacancies via engineering heterostructured Fe_3C/Fe_3O_4 catalysts for electrochemical ammonia synthesis. *Angew. Chem. Int. Ed.* **62**, e202304797 (2023).
15. Yuan, M. et al. Unveiling electrochemical urea synthesis by co-activation of CO_2 and N_2 with Mott–Schottky heterostructure catalysts. *Angew. Chem. Int. Ed.* **60**, 10910–10918 (2021).
16. Zhang, Z.-S. et al. Intrinsically active surface in a Pt/γ-Mo_2N catalyst for the water–gas shift reaction: molybdenum nitride or molybdenum oxide? *J. Am. Chem. Soc.* **142**, 13362–13371 (2020).
17. Yao, Y. et al. Carbothermal shock synthesis of high-entropy-alloy nanoparticles. *Science* **359**, 1489–1494 (2018).
18. Cao, G. et al. Liquid metal for high-entropy alloy nanoparticles synthesis. *Nature* **619**, 73–77 (2023).
19. Yao, Y. et al. High-entropy nanoparticles: synthesis–structure–property relationships and data-driven discovery. *Science* **376**, eabn3103 (2022).
20. Mei, Y. et al. MoZn-based high entropy alloy catalysts enabled dual activation and stabilization in alkaline oxygen evolution. *Sci. Adv.* **10**, eadq6758 (2024).
21. Shi, W. et al. Heterostructure engineering in high-entropy alloy catalysts. *SusMat* https://doi.org/10.1002/sus2.261 (2024).
22. Li, T. et al. Denary oxide nanoparticles as highly stable catalysts for methane combustion. *Nat. Catal.* **4**, 62–70 (2021).
23. Shi, W. et al. Transient and general synthesis of high-density and ultrasmall nanoparticles on two-dimensional porous carbon via coordinated carbothermal shock. *Nat. Commun.* **14**, 2294 (2023).
24. Yao, Y. et al. Computationally aided, entropy-driven synthesis of highly efficient and durable multi-elemental alloy catalysts. *Sci. Adv.* **6**, eaaz0510 (2020).
25. Shi, W. et al. High-entropy alloy stabilized and activated Pt clusters for highly efficient electrocatalysis. *SusMat* **2**, 186–196 (2022).
26. Sun, H. et al. Bixbyite-type Ln_2O_3 as promoters of metallic Ni for alkaline electrocatalytic hydrogen evolution. *Nat. Commun.* **13**, 3857 (2022).

27. Shen, F. et al. Oxophilic Ce single atoms-triggered active sites reverse for superior alkaline hydrogen evolution. *Nat. Commun.* **15**, 448 (2024).
28. Zhou, K. L. et al. Platinum single-atom catalyst coupled with transition metal/metal oxide heterostructure for accelerating alkaline hydrogen evolution reaction. *Nat. Commun.* **12**, 3783 (2021).
29. Wan, C. et al. Amorphous nickel hydroxide shell tailors local chemical environment on platinum surface for alkaline hydrogen evolution reaction. *Nat. Mater.* **22**, 1022–1029 (2023).
30. Zhou, S. et al. Boosting hydrogen evolution reaction by phase engineering and phosphorus doping on Ru/P–TiO_2. *Angew. Chem. Int.* **61**, e202212196 (2022).
31. Li, R. et al. New TiO_2-based oxide for catalyzing alkaline hydrogen evolution reaction with noble metal-like performance. *Small Methods* **5**, 2100246 (2021).
32. Kim, J. et al. Tailoring binding abilities by incorporating oxophilic transition metals on 3D nanostructured Ni arrays for accelerated alkaline hydrogen evolution reaction. *J. Am. Chem. Soc.* **143**, 1399–1408 (2021).
33. Hu, S. et al. Sabatier principle of metal–support interaction for design of ultrastable metal nanocatalysts. *Science* **374**, 1360–1365 (2021).
34. Vogt, C. et al. The concept of active site in heterogeneous catalysis. *Nat. Rev. Chem.* **6**, 89–111 (2022).
35. Liu, S. et al. Extreme environmental thermal shock induced dislocation-rich Pt nanoparticles boosting hydrogen evolution reaction. *Adv. Mater.* **34**, 2106973 (2022).
36. Chen, L.-N. et al. Ru nanoparticles supported on partially reduced TiO_2 as highly efficient catalyst for hydrogen evolution. *Nano Energy* **88**, 106211 (2021).
37. Kim, H. et al. Effect of hydrogen spillover on the Ru/TiO_2-catalyzed guaiacol hydrodeoxygenation: rutile vs anatase TiO_2. *ACS Catal.* **13**, 11857–11870 (2023).
38. Li, Z. et al. Oxygen-deficient TiO_2 yolk–shell spheres for enhanced lithium storage properties. *Energy Environ. Mater.* **5**, 238–244 (2022).
39. Han, B. et al. Strong metal–support interactions between Pt single atoms and TiO_2. *Angew. Chem. Int. Ed.* **59**, 11824–11829 (2020).
40. Chong, L. et al. La- and Mn-doped cobalt spinel oxygen evolution catalyst for proton exchange membrane electrolysis. *Science* **380**, 609–616 (2023).
41. Mao, Y. et al. Unravelling the synergy between oxygen vacancies and oxygen substitution in BiO_{2-x} for efficient molecular-oxygen activation. *Angew. Chem. Int. Ed.* **59**, 3685–3690 (2020).
42. Wu, Z. et al. Microwave synthesis of Pt clusters on black TiO_2 with abundant oxygen vacancies for efficient acidic electrocatalytic hydrogen evolution. *Angew. Chem. Int. Ed.* **62**, e202300406 (2023).
43. Lin, Z. et al. Reversed spillover effect activated by Pt atom dimers boosts alkaline hydrogen evolution reaction. *Adv. Funct. Mater.* **33**, 2307510 (2023).
44. Lu, Z. et al. Ultrahigh hydrogen evolution performance of under-water 'superaerophobic' MoS_2 nanostructured electrodes. *Adv. Mater.* **26**, 2683–2687 (2014).
45. Zhou, J. et al. Electrochemically accessing ultrathin Co (oxy)-hydroxide nanosheets and operando identifying their active phase for the oxygen evolution reaction. *Energy Environ. Sci.* **12**, 739–746 (2019).
46. Pan, Y. et al. Electronic structure and *d*-band center control engineering over M-doped CoP (M = Ni, Mn, Fe) hollow polyhedron frames for boosting hydrogen production. *Nano Energy* **56**, 411–419 (2019).
47. Wei, Z.-W. et al. Reversed charge transfer and enhanced hydrogen spillover in platinum nanoclusters anchored on titanium oxide with rich oxygen vacancies boost hydrogen evolution reaction. *Angew. Chem. Int. Ed.* **60**, 16622–16627 (2021).
48. Zheng, Y. et al. High electrocatalytic hydrogen evolution activity of an anomalous ruthenium catalyst. *J. Am. Chem. Soc.* **138**, 16174–16181 (2016).
49. Li, G. et al. The synergistic effect of Hf–O–Ru bonds and oxygen vacancies in Ru/HfO_2 for enhanced hydrogen evolution. *Nat. Commun.* **13**, 1270 (2022).
50. Jiang, X. et al. The heterostructure of Ru_2P/WO_3/NPC synergistically promotes H_2O dissociation for improved hydrogen evolution. *Angew. Chem. Int. Ed.* **60**, 4110–4116 (2021).
51. He, Q. et al. Achieving efficient alkaline hydrogen evolution reaction over a Ni_5P_4 catalyst incorporating single-atomic Ru sites. *Adv. Mater.* **32**, 1906972 (2020).
52. Hasegawa, M. in *Treatise on Process Metallurgy* (ed. Seetharaman, S.) Ch. 3.3 (Elsevier, 2014).
53. Weimer, A. W. et al. Kinetics of carbothermal reduction synthesis of beta silicon carbide. *AIChE J.* **39**, 493–503 (1993).
54. Reed, T. B. *Free Energy of Formation of Binary Compounds* (MIT Press, 1971).

Acknowledgements

This work is supported by the National Key R&D Program of China (grant no. 2021YFA1202300), the National Natural Science Foundation of China (grant nos. 22325901, 52371223, 52401280, 52101255 and 52272046), the Beijing National Laboratory for Molecular Sciences (BNLMS202405) and the Fundamental Research Funds for the Central Universities of HUST (grant nos. 2023JCYJ004 and YCJJ20242227). Y.S. acknowledges the 'Young Talent Support Plan' of Xi'an Jiaotong University. Supercomputing facilities were provided by Hefei Advanced Computing Center. We thank the test support from the Analytical and Testing Center of Huazhong University of Science and Technology, the State Key Laboratory of Materials Processing, and Die and Mould Technology.

Author contributions

Y.Y. and B.Y.X. conceived and designed the project. W.S. synthesized the materials. W.S., H.L., H.Z., L.Z. and K.Y. carried out the electrochemical testing. W.S., Zihui Liang, J.Z., B.Y.X. and Y.Y. contributed to the characterization and related discussion. W.S., F.T., Y.L. and Zihui Liang performed the contact angle measurements. Y.S. and S.S. contributed to the theoretical calculations. J.Z., Y.W, Y.G., D.S. and Zhiqiang Liang. contributed to the STEM measurements. Y.L. designed the roll-to-roll equipment. W.S., H.L., Y.H., B.Y.X. and Y.Y. cowrote and revised the paper. All the authors discussed the results.

Competing interests

The authors declare no competing interests.

Additional information

Supplementary information The online version contains supplementary material available at https://doi.org/10.1038/s44160-025-00758-y.

Correspondence and requests for materials should be addressed to Bao Yu Xia or Yonggang Yao.

Peer review information *Nature Synthesis* thanks the anonymous reviewers for their contribution to the peer review of this work. Primary Handling Editor: Alexandra Groves, in collaboration with the *Nature Synthesis* team.